

Laser-Driven Aerosol Synthesis of Nickel Nanoparticles

Yuanqing He, Xuegeng Li, and Mark T. Swihart*

Department of Chemical and Biological Engineering, University at Buffalo (SUNY),
Buffalo, New York 14260-4200

Received October 26, 2004. Revised Manuscript Received December 3, 2004

Nanoparticles of nickel have been prepared by laser-driven decomposition of nickel carbonyl. In this method, an infrared laser rapidly heats a dilute mixture of nickel carbonyl and a photosensitizer in a carrier gas to decompose the precursor and initiate particle nucleation. To produce nickel nanoparticles, nickel carbonyl was generated in situ from activated nickel powder and CO at room temperature, so that we never maintained any inventory of this highly toxic compound. During the synthesis process, laser heating allows for rapid cooling of the freshly nucleated particles by mixing with unheated gas. By varying the precursor flow rate, laser energy, and unheated gas flow rate to change the residence time, precursor concentration, and reaction temperature, the average particle size can be controlled over a range of primary particle diameters from 5 to 50 nm. The particle size and crystalline structure have been characterized using X-ray diffraction (XRD), transmission electron microscopy (TEM), nitrogen physisorption surface area measurement (the BET method), and X-ray photoelectron spectroscopy (XPS). Results of magnetization measurements for small superparamagnetic nickel nanoparticles (about 8-nm diameter) are also presented.

Introduction

The synthesis of nickel-based nanophase materials has attracted considerable interest because of their important potential applications¹ as pigments, catalysts,^{2,3} components of magnetic data storage media,⁴ and elements of chemical and biological sensors.⁵ Ultrafine magnetic particles^{6,7} can also be used in magnetic inks and other magnetic fluids (ferrofluids)⁸ and in biomedical applications.^{9–13} Magnetic nanoparticles are also ideal systems for fundamental research in several areas including superparamagnetism, magnetic dipolar interactions, and magnetoresistance. As a result, a significant amount of work has been done to study the preparation and magnetic properties of such particles. Several techniques have been used for the production of metallic magnetic nanoparticles, such as inert gas evaporation/condensation,^{14–17} sonochemistry,^{18,19} coprecipitation,^{20,21} wet

chemical methods,^{4,22–27} microemulsion methods,³ the polyol process,²⁸ and laser-driven thermal methods.^{16,29–31} We have also reported production of superparamagnetic iron nanoparticles by the laser pyrolysis method reported here for nickel nanoparticles.³²

There are very few reports on vapor-phase synthesis of nickel nanoparticles with diameters below 100 nm, though larger (micron diameter and larger) particles are synthesized commercially in tonnage quantities by thermal decomposition of nickel carbonyl. He et al. reported a UV laser-assisted gas-phase photonucleation process to generate nickel ultrafine

* Author to whom correspondence should be addressed. E-mail: swihart@eng.buffalo.edu; phone: (716) 645-2911 x2205; fax: (716) 645-3822.

- (1) Hyeon, T. *Chem. Commun.* **2003**, 927.
- (2) Weber, A. P.; Seipenbusch, M.; Kasper, G. *J. Nanoparticle Res.* **2003**, *5*, 293.
- (3) Guo, L.; Huang, Q.; Li, X.-y.; Yang, S. *Phys. Chem. Chem. Phys.* **2001**, *3*, 1661.
- (4) Teng, X. W.; Yang, H. *J. Am. Chem. Soc.* **2003**, *125*, 14559.
- (5) Carpenter, E. E. *J. Magn. Magn. Mater.* **2001**, *225*, 17.
- (6) Shi, J.; Gider, S.; Babcock, K.; Awschalom, D. D. *Science* **1996**, *271*, 937.
- (7) Majetich, S. A.; Jin, Y. *Science* **1999**, *284*, 470.
- (8) Raj, K.; Moskowitz, B.; Casciari, R. *J. Magn. Magn. Mater.* **1995**, *149*, 174.
- (9) Berry, C. C.; Curtis, A. S. G. *J. Phys. D: Appl. Phys.* **2003**, *36*, R198.
- (10) Tartaj, P.; Morales, M. D.; Veintemillas-Verdaguer, S.; Gonzalez-Carreño, T.; Serna, C. J. *J. Phys. D: Appl. Phys.* **2003**, *36*, R182.
- (11) Halbreich, A.; Roger, J.; N., P. J.; Geldwerth, D.; Da Silva, M. F.; Roudier, M.; Bacri, J. C. *Biochimie* **1998**, *80*, 379.
- (12) Scherer, F.; Anton, M.; Schillinger, U.; Henke, J.; Bergemann, C.; Kruger, A.; Gansbacher, B.; Plank, C. *Gene Therapy* **2002**, *9*, 102.
- (13) Pankhurst, Q. A.; Connolly, J.; Jones, S. K.; Dobson, J. *J. Phys. D: Appl. Phys.* **2003**, *36*, R167.
- (14) Choi, C. J.; Tolochko, O.; Kim, B. K. *Mater. Lett.* **2002**, *56*, 289.
- (15) Jonsson, B. J.; Turkki, T.; Strom, V.; El-Shall, M. S.; Rao, K. V. *J. Appl. Phys.* **1996**, *79*, 5063.
- (16) Ullmann, M.; Friedlander, S. K.; Schmidt-Ott, A. *J. Nanoparticle Res.* **2002**, *4*, 499.
- (17) Wu, R.; Xie, C. *Mater. Lett.* **2003**, *57*, 1539.
- (18) Kataby, G.; Koltypin, Y.; Ulman, A.; Felner, I.; Gedanken, A. *Appl. Surf. Sci.* **2002**, *201*, 191.
- (19) Jung, J.-S.; Choi, K.-H.; Chae, W.-S.; Kim, Y.-R.; Jun, J.-H.; Malkinski, L.; Kodenkandath, T.; Zhou, W.; Wiley, J. B.; O'Connor, C. J. *J. Phys. Chem. Solids* **2003**, *64*, 385.
- (20) Ge, F.; Chen, L.; Ku, W.; Zhu, J. *Nanostruct. Mater.* **1997**, *8*, 703.
- (21) Li, G.-J.; Huang, X.-X.; Ruan, M.; Guo, J.-K. *Ceram. Int.* **2002**, *28*, 165.
- (22) Dubois, E.; Chevalet, J.; Massart, R. *J. Mol. Liq.* **1999**, *83*, 243.
- (23) Bermejo, E.; Becue, T.; Lacour, C.; Quarton, M. *Powder Technol.* **1997**, *94*, 29.
- (24) Sun, Y.-P.; Rollins, H. W.; Guduru, R. *Chem. Mater.* **1999**, *11*, 7.
- (25) Chen, D.-H.; Hsieh, C.-H. *J. Mater. Chem.* **2002**, *12*, 2412.
- (26) Hou, T.; Gao, S. *J. Mater. Chem.* **2003**, *13*, 1510.
- (27) Wu, S.-H.; Chen, D.-H. *Chem. Lett.* **2004**, *33*, 406.
- (28) Wu, S.-H.; Chen, D.-H. *J. Colloid Interface Sci.* **2003**, *259*, 282.
- (29) Miguel, O. B.; Morales, M. P.; Serna, C. J.; Veintemillas-Verdaguer, S. *IEEE Trans. Magn.* **2002**, *38*, 2616.
- (30) Veintemillas-Verdaguer, S.; Bomati, O.; Morales, M. P.; Nunzio, P. E. D.; Martelli, S. *Mater. Lett.* **2003**, *57*, 1184.
- (31) Martelli, S.; Bomati-Miguel, O.; Dominicus, L. d.; Giorgi, R.; Rinaldi, F.; Veintemillas-Verdaguer, S. *Appl. Surf. Sci.* **2002**, *186*, 562.
- (32) He, Y.; Sahoo, Y.; Wang, S.; Luo, H.; Prasad, P. N.; Swihart, M. T. *J. Nanoparticle Res.* **2004**, submitted.

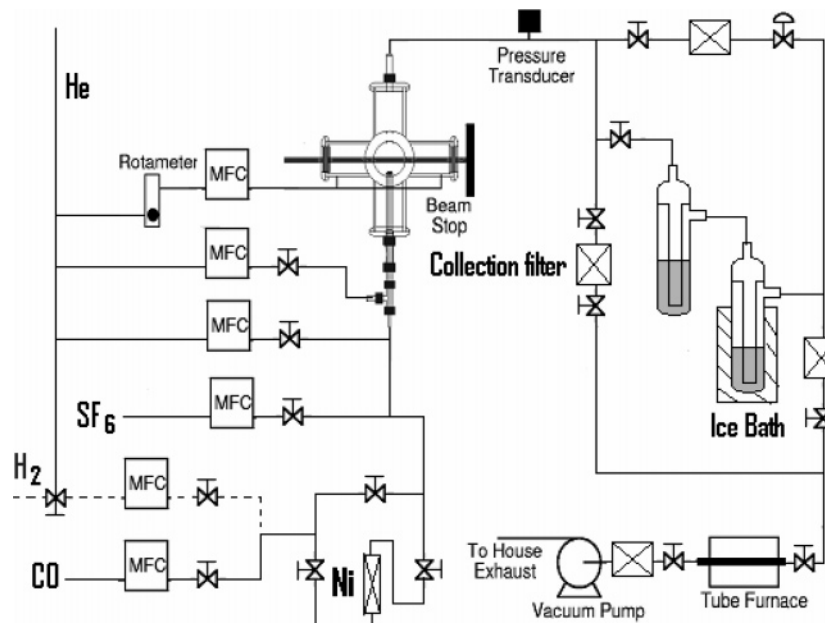


Figure 1. Schematic drawing of the reactor system for producing Ni nanoparticles by laser-driven decomposition of $\text{Ni}(\text{CO})_4$.

particles (UFPs) at ambient temperature with $\text{Ni}(\text{CO})_4$ as precursor.³³ $\text{Ni}(\text{CO})_4$ has a high vapor pressure and decomposes cleanly to give pure nickel and is therefore used in vast quantities in commercial nickel refining. However, its high toxicity has limited its use as a gaseous precursor in laboratory studies. To avoid maintaining an inventory of $\text{Ni}(\text{CO})_4$, we chose to produce nickel carbonyl from activated nickel and carbon monoxide and then immediately react it to form nanoparticles and decompose any residual precursor, so that we never maintain any inventory of the highly toxic compound.

Here, we describe experiments in which the laser-driven aerosol process was used to generate nickel nanoparticles from activated commercial nickel powders. CO_2 laser pyrolysis of different CVD precursors has proven to be a successful method for preparation of nanoparticles of a variety of materials.^{34–37} These experiments demonstrate the possibility of using this method to produce nanopowders with primary particle diameters from 5 to 50 nm at production rates of hundreds of mg per hour in a small bench-scale reactor system. For nanosize nickel, which has a low tendency to oxidize, very high surface area powders with mean particle diameter below 10 nm sometimes oxidize violently upon exposure to air. Therefore, we have used conditions that produce somewhat larger particles, 10–20 nm in average size, for studying the effects of reactor operating parameters on particle size and morphology. Magnetization measurements, on the other hand, are presented for smaller particles, 5–8 nm in diameter, since these

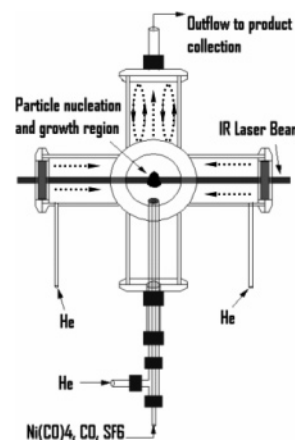


Figure 2. Schematic drawing of the reactor.

are the ones that exhibit superparamagnetism and have the most interesting magnetic behavior.

Experimental Section

The reactor configuration shown in Figures 1 and 2 was used to prepare nickel nanoparticles in the experiments described here. Because nickel carbonyl is highly toxic, we generated it in situ by flowing CO through a tube packed with nickel powder, which was placed inside of a tube furnace. This safe and convenient method was applied to generate a small flow of nickel carbonyl to the reactor without maintaining any inventory of nickel carbonyl. Details of this nickel carbonyl generator were as follows. About 605 g of nickel powder (laboratory grade, reduced powder, Fisher Chemical) was packed into a 1-in. o.d. stainless steel tube with a packed length of about 14 in.. Glass wool and a porous frit were packed at both ends to prevent the nickel powder from leaving the tube. This nickel powder was heated to 300–350 °C in a stream of flowing H_2 (250 sccm) for at least 60 min to remove any oxide on the nickel surface. The tube was then allowed to cool to room temperature under the protection of helium. A parallel line was reserved to purge the system and switch on and shut down the $\text{Ni}(\text{CO})_4$ as required. This line provided a convenient means to avoid toxic nickel carbonyl accumulation in the system. $\text{Ni}(\text{CO})_4$ was

(33) He, H.; Heist, R. H.; McIntyre, B. L.; Blanton, T. N. *Nanostruct. Mater.* **1998**, *8*, 879.

(34) Cannon, W. R.; Danforth, S. C.; Flint, J. H.; Haggerty, J. S.; Marra, R. A. *J. Am. Ceram. Soc.* **1982**, *65*, 324.

(35) Cannon, W. R.; Danforth, S. C.; Haggerty, J. S.; Marra, R. A. *J. Am. Ceram. Soc.* **1982**, *65*, 330.

(36) Li, X.; He, Y.; Talukdar, S. S.; Swihart, M. T. *Langmuir* **2003**, *19*, 8490.

(37) Li, X.; He, Y.; Swihart, M. T. *Langmuir* **2004**, *20*, 4720.

Table 1. Typical Reaction Parameters

operating pressure	SF ₆ (inlet) flow rate	SF ₆ (sheath) flow rate	He (sheath) flow rate	purge He flow rate
12.0~12.1 psia	11.9 sccm	2.6 sccm	145 sccm	1300 sccm

generated at the time of use by flowing CO through the activated bed of nickel powder at room temperature or slightly above. Exact flow rates of Ni(CO)₄ were therefore not known. After use, the tube was purged with helium for at least 30 min to remove any unreacted Ni(CO)₄ before opening the tube. A similar tube furnace at the outlet of the reactor system was used to decompose any unreacted Ni(CO)₄ to nickel film or powder before exhausting the reactor effluent.

The Ni(CO)₄ stream from the generator was typically mixed with additional helium and a small amount of sulfur hexafluoride before entering the reactor. A continuous CO₂ laser beam (Coherent, Model 42) passed directly above the central reactant inlet, which is made from 1/8-in. o.d. tubing centered within a piece of 3/8-in. o.d. tubing through which a sheath flow of helium enters the reactor. This sheath gas helps to confine the reaction zone to a small region near the axis of the reactor. In all experiments described here, the laser output was near its maximum value of 60 W. The distance between the inlet nozzle and laser beam can range from 2 to 5 mm and can be changed slightly by sliding the central tube up or down, which provides an additional means for adjustment of the reaction zone. Within a given set of experiments in which some other parameter was varied, the beam position was kept fixed. The ideal dimensions of the reaction zone are almost equal to the beam diameter, which is about 7–8 mm (1/e² power point). Sulfur hexafluoride (SF₆) is added to the precursor stream as a photosensitizer. A photosensitizer is needed because nickel carbonyl does not absorb light appreciably at the laser wavelength of 10.6 microns. SF₆ (technical grade, Aldrich) has a large absorption cross section at the laser wavelength and is stable at high temperatures. The SF₆ absorbs the laser energy and transfers it to the precursor and other gaseous molecules, resulting in very rapid heating of the gas stream. Helium (UHP, passed through an oxygen trap to remove residual O₂ and H₂O) flows confine the reactant and photosensitizer (SF₆) to a region near the axis of the reactor and prevent them from accumulating in the arms of the six-way cross from which the reactor is constructed. These helium streams entering at the ends of the horizontal arms of the reactor are referred to as the purge gas flows, while the gas entering in the outer portion of the concentric nozzle is referred to as the sheath gas in the remainder of this manuscript. If the sheath gas flow does not contain any photosensitizer, then it is not heated by the laser. Mixing of the heated particle-containing gas with this cool sheath gas and, eventually, with the purge gas, results in rapid cooling of the freshly formed particles and prevents their coalescence into larger particles. This is essential to producing small particles at high throughput. All gas flow rates to the reactor are controlled by mass flow controllers. The resulting particles are collected on cellulose nitrate membrane filters. Particles can also be collected directly into a surfactant solution using a bubbler connected in parallel with the collection filter. The solvent used for particle collection was usually toluene with surfactants (oleylamine or oleic acid) added to improve particle dispersion. Very high surface area powders, with mean particle diameter below 10 nm, sometimes oxidize violently upon exposure to air. Therefore, larger nickel nanoparticles (10~20-nm average diameter), which were more stable in air, were used for studying the effects of operating parameters on particle size and morphology. Smaller particles could be protected from oxidation by collecting them directly into surfactant solution in the bubbler. In experiments designed to produce the smallest particles (~5-nm diameter), the laser beam was focused above the precursor inlet to reduce the size of the reaction zone to 1–3 mm in diameter.

Transmission electron microscopy (TEM) was performed using a JEOL JEM 2010 microscope at an acceleration voltage of 200 kV to characterize particle size and morphology. Samples were prepared for TEM imaging as follows. Powder samples that had been collected on membrane filters were dispersed in toluene under an inert atmosphere. Multiple drops of the dispersion were cast onto a carbon-coated TEM grid and the toluene was allowed to evaporate in air. Selected-area electron diffraction was performed in the TEM to determine the crystalline structure. All TEM images shown in this manuscript were prepared from samples collected on membrane filters, but we also prepared TEM grids by evaporating drops of the dispersion of particles produced by direct collection of the particles into solution. There was no significant difference in morphology or degree of agglomeration between samples prepared in these two ways. When oleic acid or oleylamine was added to the toluene dispersions before casting them onto the TEM grid, the degree of agglomeration observed in TEM was somewhat lower. However, residual surfactant reduced the quality of both the images and the small-angle electron diffraction patterns obtained in the TEM. Specific surface area was measured by nitrogen physisorption (the BET method, Micromeritics Model 2010 ASAP Physisorption Apparatus) and was used to estimate the average particle size. Wide-angle powder X-ray diffraction (XRD, Siemens D500) was used to characterize powder samples, identifying the crystalline phases present and giving an estimate of crystalline domain size. X-ray photoelectron spectroscopy (XPS) (also called electron spectroscopy for chemical analysis or ESCA) was performed on a Physical Electronics/PHI 5300 X-ray photoelectron spectrometer for elemental analysis of the surface of the powder samples. DC magnetization measurements were made using a superconducting quantum interference device (SQUID) MPMS C-151 magnetometer from Quantum Design. The powder sample was dispersed in a high boiling solvent such as dodecane or hexadecane and put in a nonmagnetic gel capsule that was then wrapped with layers of Teflon tape to prevent breakage under vacuum. The magnetic field was ramped from 0 to 10 000 G at both 300 and 5 K.

Results and Discussion

The nickel particles collected on filters were loosely agglomerated and black in color. They were attracted to a permanent magnet, both as a powder and when dispersed in a solvent. They were readily dispersed in nonpolar solvents such as toluene or hexane, and their dispersion was improved by the addition of oleic acid or oleylamine. However, they did not form colloidal dispersions with long-term stability. Over a period of hours to days, depending on particle size, presence of surfactant, and particle preparation conditions, particles agglomerated and sedimented out of solution. This process was accelerated in the presence of a magnetic field. Many parameters such as gas flow rates, the carbonyl generator temperature, and the gases used as the photosensitizer and sheath gas can affect the nanoparticle production rate, size, and morphology.

Effect of Carbon Monoxide (CO) Flow Rate. After regenerating the nickel powder in the nickel carbonyl generator with flowing H₂ at about 300 °C, carbon monoxide (CO) can react with the active nickel surface to form nickel

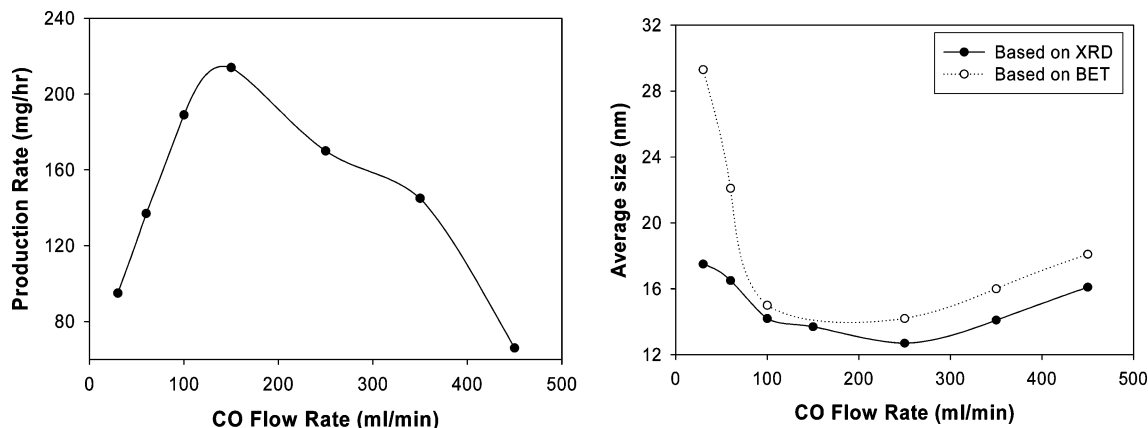


Figure 3. Nickel nanoparticle production rate and average size vs CO flow rate

carbonyl at room temperature. The concentration and flow rate of $\text{Ni}(\text{CO})_4$ into the laser-driven reactor can be changed by varying the CO flow rate, and this, in turn, affects the production rate and the average size of the nickel nanoparticles. Figure 3 shows the results that were obtained by fixing all other operating parameters and changing only the CO flow rate. The operating conditions are listed in Table 1. The average size obtained from XRD and BET experiments shown in Figure 3 are different, since XRD estimates the average crystalline domain size, but nitrogen physisorption (the BET method) measures the specific surface area of the sample. From the surface area, we calculated the average particle size assuming that the particles are spheres with the density of bulk nickel. Both of these methods of estimating average particle size show the same trend in particle size with respect to changes in the CO flow rate.

With increasing CO flow rate (from 30, 60, 100, 150, 250, 350 to 450 sccm), the production rate first increased and then decreased. This can be rationalized as follows. The main factor determining the production rate at low CO flow rates is the supply of $\text{Ni}(\text{CO})_4$ to the reactor. When the CO flow rate was lower than 150 sccm, the total supply of $\text{Ni}(\text{CO})_4$ to the reactor increased with increasing flow rate. However, when the CO flow rate increased more, even though the absolute $\text{Ni}(\text{CO})_4$ flow rate may have continued to increase, the concentration of $\text{Ni}(\text{CO})_4$ in the precursor stream decreased, if the kinetics of $\text{Ni}(\text{CO})_4$ generation from Ni and CO in the generator limited the production rate of $\text{Ni}(\text{CO})_4$. With higher flow rates, the residence time in the laser beam was shorter, and a smaller fraction of the $\text{Ni}(\text{CO})_4$ entering the reactor was converted to particles. Therefore, the production rate decreased with further increase in CO flow. For the average particle size, the residence time and $\text{Ni}(\text{CO})_4$ concentration are more important than the total supply of $\text{Ni}(\text{CO})_4$ to the reactor. With increasing CO flow rate, the residence time and $\text{Ni}(\text{CO})_4$ concentration decreased and, as a result, the average particle size decreased. When the CO flow rate was higher than 250 sccm, the average particle size increased slightly with increasing CO flow rate.

Particles were increasingly prone to deposit on the inlet nozzle at higher CO flow rates. Deposition of particles on the nozzle and reactor walls also contributed to the apparent decrease in production rate, since these particles were not collected. TEM was used to characterize the size and

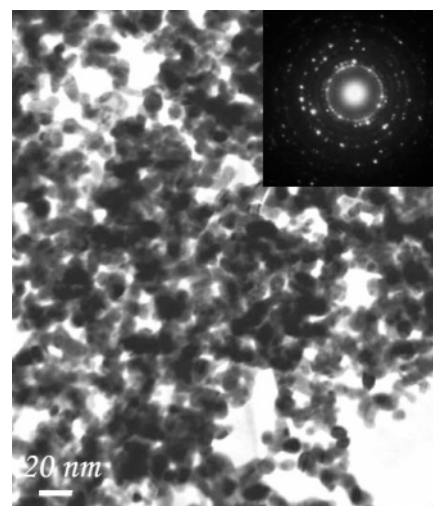


Figure 4. TEM image and selected area electron diffraction (SAED) pattern from nickel particles with 100 sccm CO flow rate.

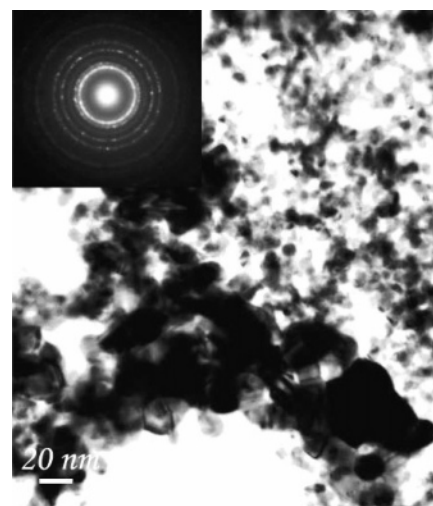


Figure 5. TEM image and selected area electron diffraction (SAED) pattern from nickel particles with 250 sccm CO flow rate.

morphology of these nickel particles. Figure 4 and Figure 5 show TEM images and selected area electron diffraction patterns (inset) from two samples produced with 100 and 250 sccm CO flow rates, respectively. The SAED pattern in Figure 5 was taken from the larger particles in the TEM image. From the TEM images, it is clear that for the larger CO flow rate, some large, agglomerated, and (partially) fused

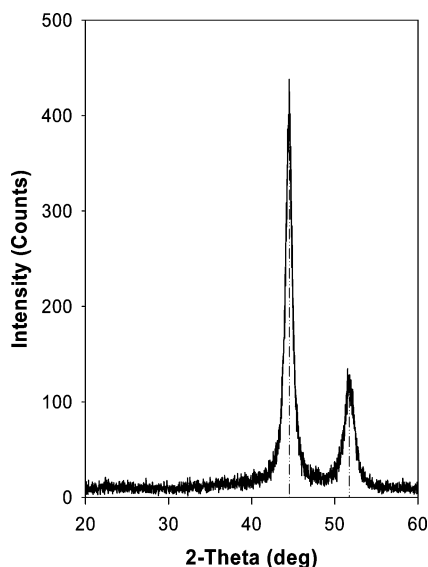


Figure 6. XRD pattern from nickel samples with 100 sccm CO flow rate.

particles are present. On the basis of these results, the increase in average particle size and the increasing tendency for particles to deposit on the inlet nozzle at high flow rates can be attributed to recirculation of gases in the top of the reactor. As shown schematically in Figure 2, there is potential for recirculation of gases in the region above the laser beam. Presumably, with increasing CO flow rate, the recirculation of mixed gases already containing nickel nanoparticles was stronger. Reheating of these recirculated particles then led to their growth and (partial) sintering to form larger particles with nonspherical shape. At the same time, some recirculated particles were deposited on the nozzle and reactor walls. The average particle size increased as a result, even as the particle size for nonrecirculated particles continued to decrease slightly.

In Figures 4 and 5, as well as other TEM images shown below, the nickel nanoparticles are substantially agglomerated. Because the particles are produced at high number concentrations, estimated to be about 10^{11} particles per cm^3 for typical conditions within the reactor, some coagulation prior to collection downstream is inevitable. Because we prepare the TEM grids from particle dispersions, it is not clear how much coagulation occurs in the reactor system and how much occurs during solvent evaporation when the TEM grids are prepared. Direct thermophoretic sampling onto TEM grids within or just after the reactor would allow this question to be addressed, but we do not currently have this capability.

Wide-angle powder X-ray diffraction (XRD) was also used to characterize all of these samples. The results were identical except for the slight changes in peak width reflected in the size estimates shown in Figure 3. Figure 6 shows the X-ray diffraction pattern from the sample that was prepared at a

CO flow rate of 100 sccm. All of these samples showed the major characteristic peaks for pure crystalline metallic nickel at 2θ values of 44.5 [Ni-111] and 51.8 [Ni-200] degrees. This indicates that there is no significant amount of crystalline NiO or other crystalline material formed and that there is not a large amount of amorphous material present, since no broad peaks indicative of an amorphous phase are observed.

Effect of the Inert Gas. An inert gas is used both as the sheath gas (entering the reactor in the concentric inlet surrounding the precursor inlet) and as the purge gas (entering the reactor at the ends of the four horizontal arms of the six-way cross) during particle synthesis. Here, experiments to compare helium (He) with argon (Ar) as sheath gas and purge gas in our system are described. Table 2 lists the operating parameters used in the experiments and the resulting production rate and mean particle size. The average size is based on XRD peak broadening.

Helium and argon have the same heat capacity, but helium has a higher thermal conductivity of about 140 mW/(m K) compared to 16 mW/(m K) for argon (at 273 K and 1 bar). Therefore, when the gas used as sheath gas and purge gas was changed, reactor conditions were significantly affected. The reaction zone temperature was increased when argon was used rather than helium. For these conditions, using argon, we could clearly observe a “flame” above the inlet nozzle, because of thermal emission from the particles produced. At the beginning of the experiment, the emission was brightest. With increasing reaction time, the “flame” turned weaker and faded. By the end of the experiment, it had almost totally disappeared. This observation is discussed in more detail below. As shown in Table 2, using helium as the sheath and purge gas led to a higher production rate and smaller average particle size than the same nominal conditions using argon as the sheath and purge gas. However, the apparent difference in production rate is based only on particles collected on the filters downstream of the reactor. When argon was used as the carrier gas, there was greater deposition of particles on the inlet nozzle and reactor walls than when helium was used. This may be the source of the apparent difference in production rate rather than any genuine change in the amount of $\text{Ni}(\text{CO})_4$ converted to particles.

XRD and TEM were also used to characterize the particles. Figure 7 shows the XRD results for the two samples. The sample produced using helium as sheath and purge gas shows only the characteristic peaks for nickel (~ 44.5 [Ni-111], and ~ 51.8 [Ni-200] degrees) particles. The sample prepared using argon as the sheath and purge gas shows not only characteristic peaks for nickel but also four more characteristic peaks at ~ 27.0 [NiF_2 -110], 34.9 [NiF_2 -101], 41.2 [NiF_2 -111], and 53.2 [NiF_2 -211] degrees, which suggests that both crystalline sulfur and nickel fluoride are present in the

Table 2. Effect of Sheath and Purge Gas Properties

Operating Pressure	SF ₆ (Inlet) Flow Rate	CO Flow Rate	Sheath Flow Rate	Purge Flow Rate
12.0~12.1 psia	4.0 sccm	100 sccm	580 sccm	1300 sccm
Experiment 1: Using Helium		Experiment 2: Using Argon		
production rate	360 mg/hr		140 mg/hr	
average size	17.4 nm		19.8 nm	

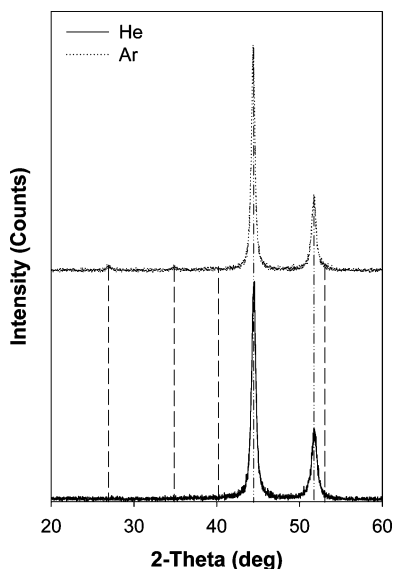


Figure 7. XRD patterns for nickel samples produced using He and Ar as sheath and purge gas.

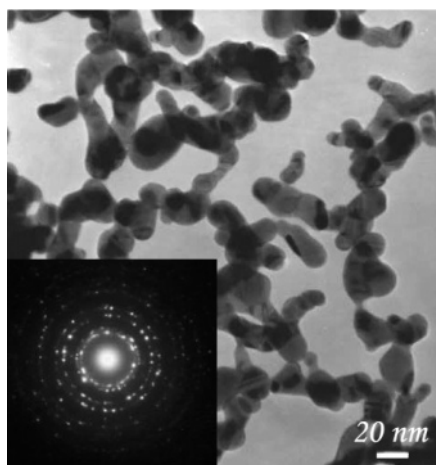


Figure 8. TEM image and SAED pattern from nickel particles produced with He sheath and purge gas.

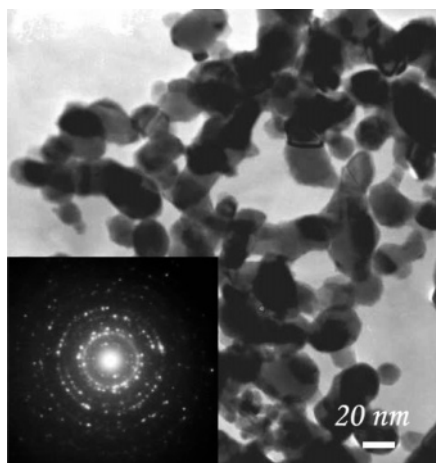


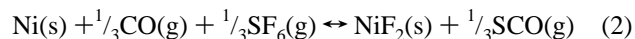
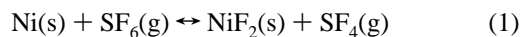
Figure 9. TEM image and SAED pattern from nickel particles produced with Ar sheath and purge gas.

sample. Figures 8 and 9 are TEM images and SAED patterns from nickel particles produced with He or Ar as sheath and purge gases, respectively. In Figure 8, most particles are smaller than 20 nm while in Figure 9 almost all the particles are larger than 20 nm, which confirms the trend shown in

the XRD results. The electron diffraction rings of the samples shown in Figure 8 and Figure 9 are consistent with the XRD results. The rings in Figure 8 can all be indexed to the cubic lattice of nickel, while in Figure 9 additional, less intense rings are present that can be indexed to elemental sulfur and to NiF_2 .

These samples were also characterized using X-ray photoelectron spectroscopy (XPS or ESCA). XPS is an extremely surface-sensitive technique that samples only the topmost 1–2 nm of the sample. As a result, it measures the composition at the particle surface and not the overall composition, even for nanoparticles of the size considered here. These measurements confirmed that the sample prepared using argon as the sheath and purge gas has a small amount of sulfur and fluorine contamination from the photosensitizer (SF_6) but that the sample made using helium as the sheath and purge gas does not. Thus, the conclusion from this section is that using argon as the sheath and purge gas can result in a higher temperature in the reaction zone, which leads to the presence of NiF_2 and sulfur in the products.

Even though SF_6 is a very stable compound, NiF_2 formation from Ni and SF_6 is a thermodynamically favorable process. Overall reactions leading to the formation of NiF_2 from Ni and SF_6 include



Reactions 1 and 2 are both exothermic, with $\Delta H_1^{\text{rxn}}(298 \text{ K}) = -194 \text{ kJ/mol}$ and $\Delta H_2^{\text{rxn}}(298 \text{ K}) = -254 \text{ kJ/mol}$. Equilibrium calculations show that, with at least a 1 to 3 SF_6 to Ni ratio, these reactions would result in complete conversion of Ni(s) to $\text{NiF}_2(\text{s})$ under all attainable reaction conditions if equilibrium were achieved. For example, an initial mixture representative of experiment two, containing 93.3% Ar, 6.1% CO, 0.29% SF_6 , and 0.27% $\text{Ni}(\text{CO})_4$, equilibrated at 0.5 bar and 1000 K gives 92.4% Ar, 0.18% SF_6 , 0.02% SF_4 , 0.08% SCO, 7.0% CO, and 0.27% NiF_2 . At higher or lower temperatures, only the amounts of SF_4 and SCO formed change. Thus, if the reaction mixture were to reach temperatures high enough for these reactions to occur on a time scale of milliseconds, we would expect to form only NiF_2 and no metallic nickel. However, SF_6 alone is stable on this time scale to temperatures of at least 1500 K and therefore is usually considered to be inert. It appears that in this system, there is some SF_6 decomposition, possibly catalyzed by the nickel nanoparticles themselves or by some gas-phase nickel-containing species.

Effect of Photosensitizer. The basic principle of this reaction system is that the laser energy is used to heat the precursor to decompose it and induce particle nucleation. $\text{Ni}(\text{CO})_4$ does not absorb at the operating wavelength of the CO_2 laser. Therefore, we must add a photosensitizer gas to the precursor stream. In addition to SF_6 , the most common sensitizer used in this method, we also used ethylene (C_2H_4 , 99.5+%, Aldrich) as a photosensitizer. Ethylene and SF_6 are both strong absorbers at 10.6 microns, however, the absolute absorbance of SF_6 is much greater than that of ethylene in

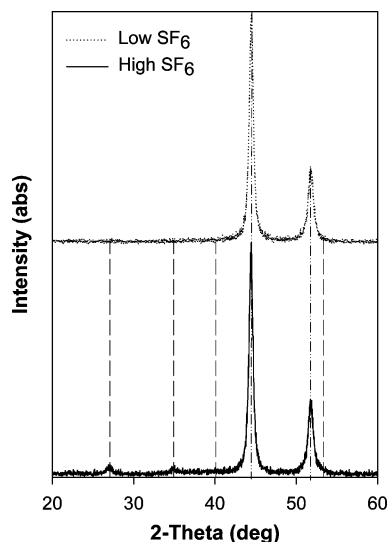


Figure 10. XRD patterns from nickel particles produced by experiment 1 and 3.

this range. Other potential photosensitizers for use with a CO₂ laser include silicon tetrafluoride (SiF₄) and ammonia. SiF₄ absorbs very strongly near 9.6 microns, and CO₂ lasers can be made to operate at that wavelength. Ammonia absorbs strongly near 10.6 microns, but the wavelength of our CO₂ laser falls between two absorption lines of ammonia, and in preliminary experiments we were not able to produce particles using it as a photosensitizer. However, it should be possible to use it as a photosensitizer with a CO₂ laser tuned to one of the many other CO₂ laser lines near 10.6 nm. Unfortunately, Ni(CO)₄ does not have any strong absorption matching the wavelength of CO₂ lasers or other lasers that can be economically used at high (tens of Watts to kilowatt) powers. On the basis of the IR absorbance spectra of SF₆ and C₂H₄, nickel particle synthesis experiments were designed. Table 3 lists the reaction conditions that were used.

Experiment 1 and 2 have been discussed above, in the context of the effect of the sheath and purge gas used. Comparing experiments 1 and 3 demonstrates the effect of SF₆ flow rate. With higher SF₆ concentration, more laser energy is absorbed, resulting in higher temperature in the reaction zone. Thus, we might expect that NiF₂ and S would be present in the product, as was the case when argon was used as the sheath and purge gas. XRD (Figure 10) and TEM (Figure 11) analyses confirmed this expectation. In Figure 10, there are four peaks at ~27.0, 34.9, 41.2, and 53.2 degrees, in addition to the nickel peaks at 44.5 [Ni-111] and 51.8 [Ni-200] degrees. These peaks correspond to NiF₂ and possibly also to crystalline sulfur. XPS experiments were again carried out to identify the elemental concentrations at the surface of the samples. Sulfur and fluorine were detected in the products from experiments 2 and 3 but not in the products of experiments 1 and 4. The fluorine concentration in sample 3 was substantially higher than in sample 2. These

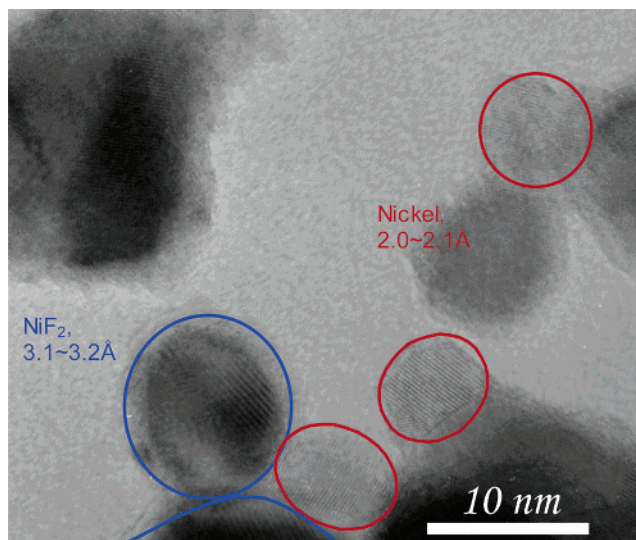


Figure 11. High resolution of TEM image of a nickel sample from experiment 3. Both nickel nanoparticles, with a lattice spacing of about 2 Å, outlined in red, and NiF₂ nanoparticles, with a lattice spacing of about 3.1 Å, outlined in blue, are present.

results confirm that using higher reaction temperature and SF₆ flow rate can lead to fluorine and sulfur contamination. Figure 11 shows a high-resolution TEM image of a sample from experiment 3, for which XRD showed that both cubic nickel and NiF₂ were present. By measuring the lattice spacing in the TEM image, we can determine which particles in the picture are nickel (lattice spacing of 2.0~2.1 Å) and which are NiF₂ (lattice spacing of 3.1~3.2 Å), thus confirming that discrete Ni and NiF₂ particles are formed rather than Ni/NiF₂ composite particles or core-shell structures.

In experiment 4, nickel particles were produced using ethylene (C₂H₄) as the photosensitizer. In this case, of course, sulfur (S) and fluorine (F) were not found in the products. To compare experiment 4 with experiment 2, XRD and TEM results are shown in Figures 12 and 13. In Figure 12, there are a total of nine characteristic peaks in the two spectra shown, for which the 2-θ values are 27.1, 34.9, 39.1, 40.1, 41.5, 44.6, 51.8, 53.1, and 58.4 degrees (from left to right). All of these peaks can be indexed to four crystal structures: NiF₂ (27.1 [NiF₂-110], 34.9 [NiF₂-101], 40.06 [NiF₂-111], and 53.06 [NiF₂-211] degrees), cubic Ni (44.507 [Ni-111] and 51.8 [Ni-200] degrees), hexagonal Ni (39.1 [Ni-010], 41.5 [Ni-002], 44.5 [Ni-011], and 58.4 [Ni-012] degrees) and sulfur (27.08 [S-222] degrees). Combining the discussion of experiment 4 with that in section 3.2, it can be concluded from XRD results that, when C₂H₄ was used as photosensitizer, both hexagonal and cubic nickel were produced. This conclusion is also supported by the SAED pattern in Figure 13. The ring diameters were measured as 9.6 mm (only several dots shown in the picture with low intensity), 10.2 mm (a clear ring with many bright dots), 11.8 mm (a ring with many dots), and 13.1 mm (several dots). This

Table 3. Reaction Parameters Used to Study the Effect of the Photosensitizer Gas

system pressure: 12~12.1 psia, CO flow rate: 100 sccm	
(1) SF ₆ (inlet):	~4 sccm, He (sheath): ~580 sccm, He (purge): ~1300 sccm
(2) SF ₆ (inlet):	~4 sccm, Ar (sheath): ~580 sccm, Ar (purge): ~1300 sccm
(3) SF ₆ (inlet):	~11.9 sccm, SF ₆ (sheath): ~2.6 sccm, He (sheath): ~580 sccm, He (purge): ~1300 sccm
(4) C ₂ H ₄ (inlet):	~150 sccm, Ar (sheath): ~364 sccm, Ar (purge): ~1300 sccm

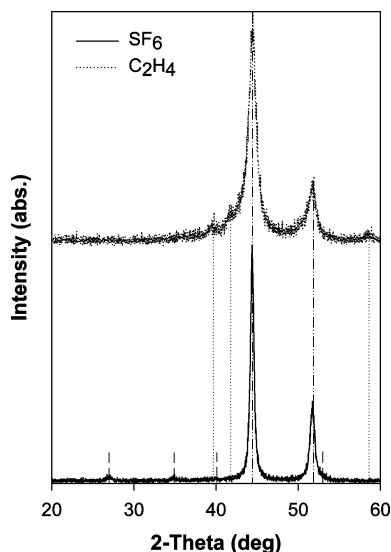


Figure 12. XRD patterns from nickel particles produced by experiment 2 and 4.

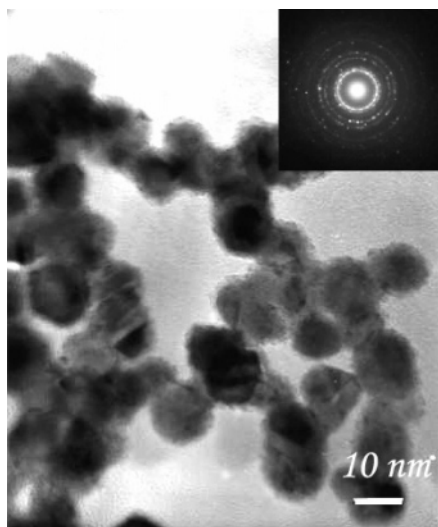


Figure 13. TEM image and SAED pattern from nickel particles produced with C_2H_4 as photosensitizer.

indicates that hexagonal nickel (9.6, 10.2, and 13.1 nm) and cubic nickel (10.2 and 11.8 nm) are present in the sample from experiment 4. Comparing Figure 13 with other TEM images, it is found that when C_2H_4 was used as the photosensitizer, the particles are relatively spherical, showing less sintering and necking compared with samples produced using SF_6 as the photosensitizer. We also observed that the particles produced with C_2H_4 as the photosensitizer were much more readily dispersed in nonpolar solvents such as toluene or hexane than the particles produced using SF_6 . Both the decreased sintering and improved dispersibility may result from the presence of carbon on the particle surface. No graphite phase was seen in the XRD or SAED results, but it is still possible that a small amount of amorphous carbon is present on the particle surface. It was not possible to use XPS to determine whether carbon was present, because substantial carbon and oxygen contamination was seen in the XPS spectra of these high surface area nanoparticle samples for all conditions.

Effect of Precursor Concentration. To supply $Ni(CO)_4$ to the reactor, we used reaction of CO with activated nickel

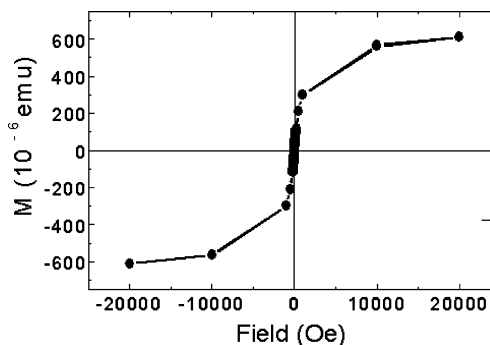


Figure 14. Magnetization measurements on a nickel nanoparticle sample, showing magnetization without hysteresis at 300 K.

powder to generate $Ni(CO)_4$ just upstream of the particle synthesis reactor. Therefore, in addition to the CO flow rate, there are also other factors that influence the $Ni(CO)_4$ supply to the reactor, such as the amount of nickel powder inside the generator, the state of the nickel powder surface, and the temperature in the generator. The effects of temperature and of hydrogen activation of the nickel surface were studied qualitatively. Silicone rubber extruded heating tape (SRT Series, Omega) was used to heat the bottom of the generator tubing (outside the furnace) until the temperature at that location stabilized at 77 °C while Ar gas was flowing through the tubing. The furnace itself was not heated but simply served as insulation to maintain the temperature inside the generator. The experimental details and results are listed in Table 4.

If particles were made with the generator at room temperature, the production rate decreased with time (starting from freshly regenerated powder in the generator), which indicates that activation state of the nickel surface can affect the $Ni(CO)_4$ concentration delivered. With increasing time online, after regeneration, the $Ni(CO)_4$ production rate decreased. This explains why the flame was weaker and faded with increasing the reaction time. Lower $Ni(CO)_4$ concentration also results in smaller nickel particles. When the precursor tubing was heated, the rate of conversion of nickel powder to $Ni(CO)_4$ in the generator increased. Therefore, the production rate with the generator slightly heated is greater than that with the generator at room temperature. Again, the production rate decreased with time online. However, the average size from XRD measurements did not show any meaningful trend in particle size accompanying the change in production rate caused by changing the temperature of the carbonyl generator.

Other Factors. There are several other factors that affect the synthesis process, including laser position (relative to the inlet nozzle), sheath and purge gas flow rates, and operating pressure. Lower laser beam position tends to make larger particles because there is less diffusion of $Ni(CO)_4$ into the surrounding gas before reaching the laser beam. This effectively increases the $Ni(CO)_4$ concentration in the reaction zone. Larger sheath and purge gas flow rates lead to shorter residence time in the reaction zone, which results in decreased particle size. Decreasing the operating pressure lowers the concentration of both precursor and photosensitizer, decreases the residence time, and increases diffusion of precursor and photosensitizer out of the laser-heated

Table 4. Effect of Carbonyl Generator Temperature and Time Online

experiment 1		experiment 5		
with carbonyl generator at room temperature		with carbonyl generator heated		
1st hour	2nd hour	1st hour	2nd hour	3rd hour
357 mg/hr	235 mg/hr	506 mg/hr	394 mg/hr	344 mg/hr
17.4 nm	15.4 nm	17.8 nm	18.6 nm	18.1 nm

Table 5. Reaction Parameters and Results (Effect of Operating Pressure)

He (sheath) flow rate	SF ₆ (inlet) flow rate	CO flow rate	purge He flow rate
580 sccm	4.0 sccm	100 sccm	1300 sccm
experiment 1: operating pressure 11.9~12.0 psia		Resulting particles: ~17.4 nm	
experiment 6: operating pressure 7.9~8.0 psia		Resulting particles: ~15.4 nm	
experiment 7: operating pressure 5.9~6.0 psia		Resulting particles: ~14.2 nm	

Table 6. Typical Reaction Parameters for Making Small Nickel Nanoparticles

Experiment (10)					
operating pressure	SF ₆ (inlet) flow rate	CO flow rate	He (inlet) flow rate	He (sheath) flow rate	purge He flow rate
8.4~8.5 psia	4.0 sccm	30 sccm	55 sccm	320 sccm	2545 sccm

region. Thus, it tends to decrease the average particle size. Table 5 shows the effect of decreasing total pressure on the particle size, as determined by XRD peak broadening.

Methods to Measure Ni(CO)₄ Concentration. As described above, the exact Ni(CO)₄ concentration entering the reactor from the carbonyl generator was not known. However, the nickel carbonyl concentration and delivery rate is a key parameter in determining particle size, production rate, and efficiency of the system in converting nickel carbonyl to nickel powder. Here, we describe one method used to obtain an approximate measurement of the Ni(CO)₄ delivery rate. A sample flow of the nickel carbonyl containing gas was diverted into two bubblers in series containing a bromine/alcohol solution. The nickel carbonyl dissolved in the alcohol and quickly reacted with the bromine to form NiBr₂. The bubbler solution was collected and analyzed to determine the nickel content. The carbonyl concentration in the original gas sample was then calculated using the amount of nickel collected, the gas flow rate, and the gas collection time. The configuration was like that shown in Figure 1, except that only the collection bubbler line was open, and the powder collection line was closed. During sampling, the laser was shut down and the stream containing Ni(CO)₄ and CO was mixed with He to control the operating pressure at around 11.7psi. The flow rate of CO through the precursor tubing was 100 sccm with 580 sccm He as the sheath gas and 1300 sccm He as purge gas (nominally the same conditions as experiment 1, but with the laser turned off). After using He gas to carefully purge the system, contents of both bubblers were mixed together in a flask, and the solvent and unreacted bromine were evaporated. Nitric acid (~70%) was added to dissolve the NiBr₂ salt remaining in the flask, and a clear green NiBr₂ solution was obtained. The resulting sample contained 0.6145 g of nickel. This corresponds to a Ni(CO)₄ delivery rate of 1.43 g/h, or 0.008 mol/h, or 3.1 sccm. About 13% of the CO entering the generator was converted to nickel carbonyl for these conditions (room temperature). Comparing this delivery rate to the production rate shown in Table 4 during an experiment using nominally the same conditions with the laser turned on, it is estimated that 60–70% of the Ni(CO)₄ delivered to the reactor was converted to particles.

Magnetic Properties of Nickel Nanoparticles. Nickel is, of course, ferromagnetic as a bulk material. However, the smallest particles produced here are expected to be superparamagnetic. Here, we present a single result demonstrating the superparamagnetic behavior of one sample of nickel nanoparticles. A more complete and detailed analysis of the magnetic properties of the nickel nanoparticles will be presented separately.³⁸ Measurements of the magnetization of particles produced in experiment 10, under the conditions listed in Table 6, are shown in Figure 14. The particles showed typical superparamagnetic behavior, with no hysteresis at 300 K and a high saturation field of about 2 T.

Summary and Conclusions

Laser-driven pyrolysis of nickel carbonyl was used to produce nickel nanoparticles. A safe, convenient method was implemented to supply a small flow of nickel carbonyl for laser-induced synthesis of nickel particles. Hydrogen-regenerated nickel powder and carbon monoxide were used to prepare nickel carbonyl in a stream that flowed directly to the reactor and was immediately decomposed back to nickel and CO. While this carbonyl generation method was convenient for producing small amounts of very small nickel nanoparticles, it limited the experiments to relatively low Ni(CO)₄ concentrations. In the present study, factors that affect the nickel particle size, production rate, and morphology were considered. TEM images, selected area electron diffraction patterns, XRD, BET, and XPS (ESCA) analysis were used to characterize particles. Particles ranging from 5 to 50 nm in average diameter were obtained. CO flow rate affects particle size as well as production rate in this system by changing the Ni(CO)₄ concentration and delivery rate and, at high flow rates, by altering the flow patterns in the reactor and inducing recirculations. The choice of inert gas used for sheath and purge flows affects the temperature in the reaction zone via the thermal conductivity and heat capacity of the gas. Higher temperature leads to appearance of a visible flame in the reaction zone. Both SF₆ and C₂H₄ can be used as photosensitizers. When using a relatively high SF₆ flow

(38) Sahoo, Y.; He, Y.; Swihart, M. T.; Wang, S.; Luo, H.; Furlani, E. P.; Prasad, P. N. *Phys. Rev. B* **2004**, submitted.

rate, which leads to relatively high temperature in the reaction zone, F and S were present in the sample as NiF_2 and elemental sulfur. Use of C_2H_4 as the photosensitizer changes the particle morphology and crystal structure as well as eliminating S and F contamination. Laser position and power, inert gas flow rate, and operating pressure can also be used to vary particle size and production rate. In magnetization measurements, powder samples of nanoparticles about 8 nm in diameter showed magnetization without hysteresis at room

temperature. That is, they are superparamagnetic at room temperature, as is expected for such small particles.

Acknowledgment. We thank Dr. Y. Sahoo for many helpful discussions and Prof. H. Luo and S. Wang for performing the magnetization measurements. This work was partially supported by a grant from the University at Buffalo (SUNY) Office of the Vice President for Research.

CM048128T